In-plane mode dynamics of capillary self-alignment

Langmuir

Article

pubs.acs.org/Langmuir

In-Plane Mode Dynamics of Capillary Self-Alignment

Gari Arutinov,[†,‡,§] Edsger C. P. Smits,[‡] Pierre Albert,[‡] Pierre Lambert,[∥] and Massimo Mastrangeli*[,†,∥]

[‡]Holst Centre, TNO, High Tech Campus 31, 5656 AE Eindhoven, Netherlands

[§]Microsystems, Eindhoven University of Technology, De Wielen, 5612 AZ Eindhoven, Netherlands

[∥]Bio-, Electro- and Mechanical Systems (BEAMS), École Polytechnique de Bruxelles, Université Libre de Bruxelles, 1050 Brussels, Belgium

Supporting Information

ABSTRACT: We present an experimental study of the complete in-plane dynamics of capillary self-alignment. The two translational (shift) and single rotational (twist) in-plane modes of square millimetric transparent dies bridged to shape-matching receptor sites through a liquid meniscus were selectively excited by preset initial offsets. The entire self-alignment dynamics was simultaneously monitored over the three in-plane degrees of freedom by high-speed optical tracking of the alignment trajectories. The dynamics of the twist mode is shown to qualitatively follow the sequence of dynamic regimes also observed for the shift modes, consisting of initial transient wetting, acceleration toward, and underdamped harmonic oscillations around the equilibrium position. Systematic analysis of alignment trajectories for individually as well as simultaneously excited modes shows that, in the absence of twist offset, the dynamics of the degenerate shift modes are mutually independent. In the presence of twist offset, the three modes conversely evidence coupled dynamics, which is attributed to a synchronization mechanism affected by the wetting of the bounding surfaces. The experimental results, justified by energetic, wetting, and dynamic arguments, provide substantial benchmarks for understanding the full dynamics of the process.

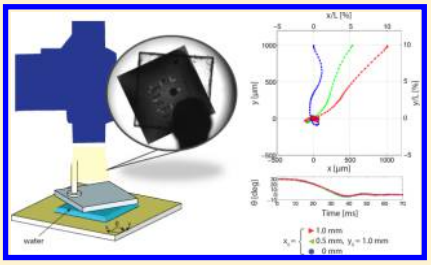

1. INTRODUCTION

Capillary self-alignment[1] is a fluidic process whereby the relaxation of a deformed liquid bridge[2] into its state of minimal energy drives bounding mobile surfaces into mutual alignment.[3] The process is ubiquitous in the presence of capillary interfaces[4,5] and particularly effective at millimetric and sub-millimetric scales, dominated by surface tension effects.[6,7] At these scales, capillary self-alignment has indeed found relevant technological applications in the fabrication and packaging of microelectronic devices,[8−10] self-assembly of microsystems,[6,11,12] and as a passive complement to robotic micro-handling[13] for highly accurate micropositioning tasks.[10,14,15] In such applications, a confined liquid meniscus[2,16,17] pulls a floating component into alignment with a receptor site.[18] The site can be part of another component[19,20] or a predetermined target position patterned onto a templated carrier.[8,9] The shape of the menisci as a function of the geometry of the bounding surfaces[21−24] as well as the ensuing capillary forces[1,24−26] and torques[1,27,28] driving capillary self-alignment have been the object of intense analytical and numerical modeling for decades.[29] Several physical and geometrical parameters have influence on the yield, throughput, and accuracy of the process, notably the geometry of the components,[18,28,30,31] the physical properties of the liquid (surface tension,[7,23] volume,[32,33] density, and viscosity[22,34−36]), the height and curvature of the meniscus,[2,17,22] the initial offsets,[24,37] the type of meniscus confinement,[16,38−40] the wettability of the bounding surfaces,[15,41,42] and the presence of wetting defects.[3,23] A number of models and experimental investigations have been reported to describe the dynamics of capillary self-alignment.[22,35,36,42−44] Nonetheless, a comprehensive explanatory framework is missing, because the majority of studies in the literature has focused primarily on energetics.[1,24,26] The latter develops a geometric quasi-static approach which, while consistently supported by experimental data,[25] captures only partially the intrinsically dynamic nature of the process.[45] The liquid bridge can in fact be deformed along six degrees of freedom (DOFs), which are associated with the three translational and three rotational DOFs of the top floating component (Figure 1). Each type of deformation (or mode) is opposed by a corresponding restoring capillary force[25] (for translational modes, i.e., shifts and lift) or torque[27] (for rotational modes, i.e., twist and tilts) tending, with the possible exception of the tilt modes,[1] to bring the system back to its configuration of global equilibrium. The mass of the meniscus and component, in combination with the stiffness associated with the modes, determines, in turn, the characteristics of the oscillations that the system undergoes along each DOF.[22,36,42,44] However, experimental and theoretical investigations have typically addressed each of the six degrees of freedom individually and, hence, disregarded the possibility of mutual influences (i.e., coupling) among simultaneously excited modes.

Received: July 18, 2014
Revised: September 16, 2014
Published: October 9, 2014

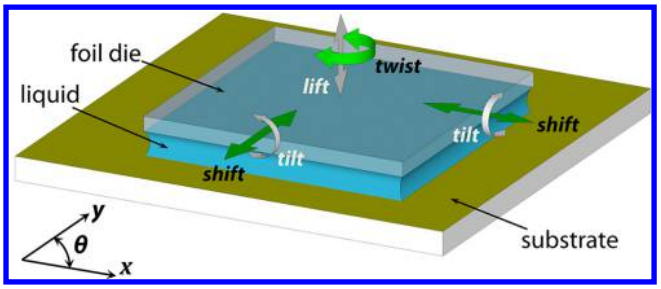

Figure 1. Translational (lift and shifts) and rotational (twist and tilts) DOFs of a transparent component floating on a confined liquid bridge (sketch not to scale). In-plane modes (shifts along x and y, twist along θ) are highlighted in green.

In this paper, we present a systematic experimental study of the in-plane dynamics of capillary self-alignment for millimeter-sized square components. Innovative designs of metrology markers laser-scribed on transparent plastic components (section 2) enable synchronous analysis of the trajectories described by the components released onto confined water menisci of optimized thickness.[37] The real-time dynamics of self-alignment was simultaneously monitored along all three in-plane DOFs, i.e., translational (x and y) and rotational (θ) (see Figure 1), by high-speed optical tracking. The synoptic view of the projections of the trajectory along the individual DOFs was used to analyze the time evolution of the process with unprecedented accuracy. In the experiments (section 3), the modes of interest were selectively excited by presetting non-null offsets along the corresponding DOFs. The number of simultaneously excited modes was progressively incremented, and trajectories of increasing dimensionality and complexity were consequently recorded. Hence, the cumulative effect of the simultaneous excitation of multiple modes on the dynamics of the process could be assessed. The results corroborate a fundamental difference and an interaction between shift and twist dynamics in capillary self-alignment, and a significant effect of the wettability of the bounding surfaces on the coupling between the in-plane modes. Finally, although the dimensions of the dies were chosen mainly for ease of imaging, qualitative insights gained from the study can readily be extrapolated to components of smaller sizes.

2. MATERIALS AND METHODS

2.1. Carrier Substrates and Foil Dies. Au-sputtered Si substrates were patterned with marked SiO_2 hydrophilic receptor sites through photolithography and wet etching (see Figure S1a of the Supporting Information). The Au surface was rendered reproducibly hydrophobic by selective functionalization with a perfluorodecanethiol self-assembled monolayer (SAM). The fabrication process is detailed in an earlier publication.[37] Static water contact angles (CAs) on hydrophobic spacer and hydrophilic receptor surfaces were 120° ± 3° and 8° ± 2°, respectively. The wetting contrast was tailored to enhance chemical edge confinement of the liquid menisci inside the receptor sites.[16]

Optically transparent square dies of sidelength L = 10 mm (see Figure S1b of the Supporting Information) were fabricated from 250 μm thick polyethylene naphthalate (PEN) foils realized by laminating two commercially available 125 μm thick PEN sheets (Teonex Q65FA, DuPont; mass density, 0.18 mg/mm^2). Water CAs on native PEN surfaces were 65° ± 3° (static) and 60° ± 2° (receding) and 9° ± 3° (static) on PEN surfaces exposed to oxygen plasma (60 s, 400 W) to increase their wettability.[42] A nanosecond Nd:YAG laser source (Coherent AVIA, 355 nm, 25 ns) combined with a galvo scanner was used for patterning and dicing the foil dies.[15] The size of the dies was chosen to best suite the optical visualization and tracking of the self-alignment dynamics and consistently with system-in-foil applications.[15,37] Several equal-sized dies were fabricated, and in each type of experiment, a single die from the set was repeatedly used.

Static and receding contact angles were measured by the static and contracted sessile drop methods, respectively (EasyDrop, KRÜSS).

A 125 μm thick layer of deionized water was precoated over the receptor sites shortly before the experiments. The water film was pinned at all edges of the sites, except for their corners.[16] The thickness of the water layer, also indicated in the following as the height or gap of the meniscus, was estimated by the deposited water volume and the area of the receptor sites. It was chosen to optimize the self-alignment process.[37]

2.2. Experimental Platform. An overview of the experimental platform is shown in Figure S2 of the Supporting Information. A base stage (XYZ 500 TIS, Quater Research and Development) with external vacuum tweezers (SMD-VAC-HP, Vacuum Industries, Inc.) providing 10 μm resolved displacements along three coordinate axes was used to pre-position the foil dies onto the receptor sites. The micropositioner held the dies about 1.5 mm above the water film. Through the circular and caret-shaped (∧) markers (see Figure S1b of the Supporting Information), the foil dies were pre-aligned on the corresponding receptor sites with predefined offsets $[x_0\ y_0\ \theta_0]' = \vec{X}_0$ and an estimated accuracy of 20 μm and 0.5°, respectively. High-speed recording started right before the foil die was released from the tweezer by the pedal-operated vacuum system. Upon release, the die landed horizontally on the water layer with macroscopically unnoticeable deviations from preset offsets. The full alignment dynamics was tracked in real time by a high-speed camera (Redlake HS-3, operated at 1000 fps; videos available in the Supporting Information) combined with a microscope stage (Leica DMLP).

2.3. Data Processing. High-speed recorded videoframes were post-processed as follows (refer to Figure S3 of the Supporting Information): (1) Raw grayscale frames (see Figure S3a of the Supporting Information) were converted to binary black and white (BW) frames (see Figure S3b of the Supporting Information) by thresholding. The chosen threshold value of pixel luminance rendered the complete marker structures clearly visible on each frame. (2) MATLAB-based processing of the BW frames returned the coordinates of the center of the circles with respect to the field of view of the camera (see Figure S3c of the Supporting Information). From this, the instantaneous position and orientation (i.e., pose) of the die $\vec{X}(t^*) = [x(t^*)\ y(t^*)\ \theta(t^*)]'$ with respect to the framing receptor site were reconstructed. The complete in-plane translational $[x(t), y(t)]$ and rotational $[\theta(t)$, around the vertical axis] motions of the die were finally computed from the analysis of the entire sequence of frames recorded for each experiment.

Each type of experiment was repeated at least 3 times. For each experiment type, the corresponding mean value and standard deviation of the coordinates of the die were computed at each sampling time out of the full set of available measurements.

2.4. Finite Element Model. A quasi-static finite element model of the confined liquid bridge was implemented in Surface Evolver[46] (SE). The water liquid bridge had surface tension γ = 72 mN/m, density ρ = 1000 kg/m^3 [capillary length $L_c = (\gamma/\rho g)^{1/2}$ = 2.7], and gap h = 125 μm. It was constrained within horizontal square pads matching the dimensions (L = 10 mm, and thickness = 250 μm) and density (1440 kg/m^3) of the foil dies. The top and bottom pad represented the floating die and the receptor site, respectively. Water CAs correspondingly reproduced those measured on native PEN and hydrophilic receptor sites (see section 2.1).

The simulations proceeded by the displacement of the floating pad from the equilibrium position. A uniaxial shift was simulated within the $0 \le x \le 1000$ μm range with steps of 5 μm. Twist was simulated within $0° \le \theta \le 45°$ in steps of 1°. Mesh refinement and optimization were implemented as described earlier.[25,45] For every top pad pose, h was updated through a local-search routine based on Newton's method to keep the system in local equilibrium.[21] The non-constancy of $h(x,y,\theta)$ was implemented for physical consistency with (1) time scale separation, because of the dominance of vertical over lateral

dx.doi.org/10.1021/la502831r | Langmuir 2014, 30, 13092−13102

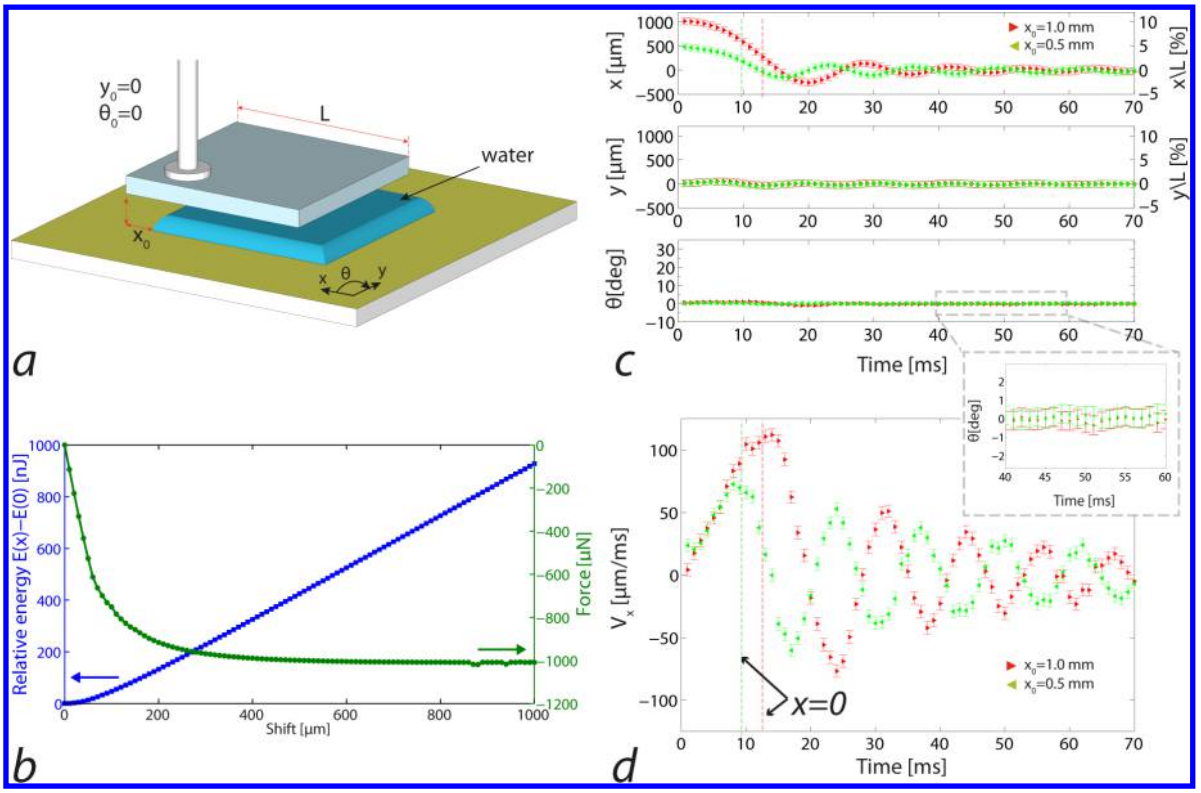

Figure 2. Uniaxial shift. (a) Sketch of experimental procedure (not to scale). (b) Relative energy landscape and capillary restoring force predicted by quasi-static SE simulation of the uniaxial shift mode. (c) Modal trajectories under uniaxial shift dynamics ($x_0 > 0$, and $y_0 = \theta_0 = 0$). (d) Corresponding die velocity V_x along the individually excited shift mode. This case subsumes the analysis of uniaxial capillary self-alignment developed in a previous work.[42]

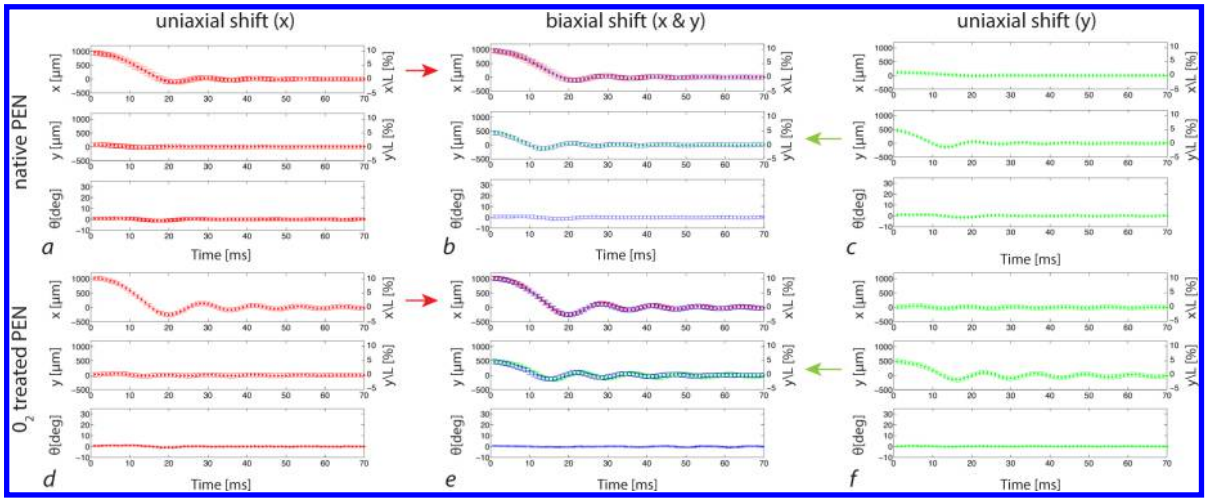

Figure 3. Independence of the dynamics of the orthogonal shift modes in the absence of twist offset. Uniaxial shift trajectories for x ($x_0 = 1000$ μm, $y_0 = 0$ μm, and $\theta_0 = 0°$) and y ($x_0 = 0$ μm, $y_0 = 500$ μm, and $\theta_0 = 0°$) are shown in the first and third columns, respectively. Biaxial trajectories for the same offsets ($x_0 = 1000$ μm, $y_0 = 500$ μm, and $\theta_0 = 0°$) are shown in the central column, pointwise superposed with the trajectories of the individual shift modes. The coincidence of the dynamics of the individually excited modes with the projections of the two-dimensional biaxial dynamics along the individual DOFs is indicated by corresponding horizontal arrows. Mutual independence of shift modes is unaffected by the surface energy of the die, as exemplified for the cases of native PEN (top row) and oxidized PEN foil die (bottom row).

capillary forces for this system,[3] (2) the tendency of the liquid bridge to assume the geometry locally closest to a section of a sphere,[21,23] and (3) conservation of the meniscus volume, which upon contact line unpinning(s) induces an increase of h to partially compensate for the decrease of wet pad surface(s).[45] After setting h, the restoring capillary force and torque were computed by the method of virtual works[47] implemented using central finite differences.

3. RESULTS

3.1. Uniaxial Shift Dynamics. Modal trajectories of the experimental uniaxial shift dynamics (i.e., $x_0 > 0$, and $y_0 = \theta_0 = 0$; Figure 2a) of capillary self-alignment of the native PEN die are illustrated in Figure 2. The enhanced representation of the process enabled by our metrology framework (see section 2)

dx.doi.org/10.1021/la502831r | Langmuir 2014, 30, 13092−13102

can be appreciated for this instance by comparison to a previous experimental analysis of the uniaxial shift mode.[42]

Figure 2c shows trajectories for initial shifts of 500 and 1000 μm, corresponding to 5 and 10% of the die sidelength, respectively. For both offset values, the single-shift mode was effectively excited and the sequential dynamic regimes[42] of transient wetting, constant acceleration, and underdamped harmonic oscillations were clearly observed. It can be seen, as also reported before,[42] that a larger initial offset of the die induces a slight corresponding delay in the first crossing of the equilibrium position (referred to as first zero crossing in the following; Figure 2c). The acceleration that the die attains along the direction of motion is identical for both offset values (Figure 2d). This evidence is consistent with the energetic description of the water meniscus provided by the SE model of the uniaxial shift mode (Figure 2b). The simulation shows that, for both offset values adopted in the experiments, the initial capillary force acting on the die has nearly the same value and remains almost constant until reaching close proximity of the rest position, i.e., less than 5% of the sidelength in the present case, with the actual limit being sensitive to the energies of the solid surfaces. This analysis justifies the linear velocity approximation used to describe the die in its parabolic dynamic regime.[42] We recently proposed an analytical quasi-static description of the uniaxial shift mode, accounting for relatively large deformations of the meniscus as imposed in the present study and for partial wettability of the bounding surfaces.[45] Even larger relative shift offsets (e.g., more than 30% of the sidelength) can nonetheless be successfully used, as demonstrated in a collateral work.[15] The effect of die surface energy on shift dynamics is described in the next section with respect to the biaxial shift case.

Minor uncorrelated oscillations were simultaneously detected along the orthogonal shift and the twist DOFs, despite nominally null offsets (see Figure 2c and inset thereby). Such unintended oscillations were observed in the present and the incremental cases reported below. Their origin is discussed in section 4. For practical purposes, the negligible magnitude of these oscillations provided a signature to assess the absence of coupling in the dynamics of the mode under the imposed boundary conditions.

3.2. Biaxial Shift Dynamics. Modal trajectories for experimental capillary self-alignment under biaxial shift offset (i.e., with both shift modes excited simultaneously) and in the absence of twist offset are depicted in the central column of Figure 3. The first and third columns of the same picture show the trajectories of individually excited uniaxial shift modes for the same x_0 and y_0 offsets, respectively. In the central column, the trajectories of the individually excited shifts are additionally shown to pointwise superpose to the projections of the two-dimensional biaxial self-alignment trajectory along the single corresponding DOFs (correspondences are indicated by the horizontal arrows). This provides experimental evidence of exact decomposition of the biaxial shift trajectory into corresponding uniaxial shift trajectories. That means equivalently that, given the same boundary conditions, the trajectory described by a floating die under biaxial shift capillary self-alignment can be exactly reconstructed by the pointwise composition of the uniaxial shift trajectories described by the same die when the shift modes are individually excited with the same offsets. Minor unintended oscillations are observed along the unexcited twist DOF in this as in the uniaxial shift case described in section 3.1. Hence, within experimental accuracy, the dynamics of the orthogonal shift modes in the absence of twist offset are mutually independent. This, in turn, implies the exact decomposibility of the capillary potential field $U(x,y)$, such that, for in-plane offsets $0 \leq x_0, y_0 \ll L$, it holds that $U(x_0,y_0)|_{\theta_0=0} = U(x_0,0)|_{\theta_0=0} + U(0,y_0)|_{\theta_0=0}$. Fair evidence of the decomposibility of $U(x,y)$ comes from SE simulations, as described in the Supporting Information. We stress that such structure underlying U is by itself necessary yet not sufficient to justify the reported decomposibility of the biaxial trajectories.

Figure 3 also provides evidence that the independence of the trajectories along the shifts does not seem affected by changes in the surface energy of the foil die. The exact trajectory reconstruction described above holds for the case of foil with both a native PEN surface (top row) and an oxygen plasma-treated PEN surface (bottom row). The effect of increased foil wettability (i.e., higher surface energy) is detected in the faster motion and higher amplitude of oscillatory overshoots for the oxidized foil die versus the native foil die, as a consequence of larger driving capillary forces. This evidence is consistent with earlier experimental observations and SE simulations of uniaxial shift.[42]

The independence of a uniaxial shift trajectory on the offset applied along the orthogonal shift direction implies the independence of the capillary forces acting along these directions of motion in the absence of twist offset. This observation is striking when considering that the capillary force field associated with the meniscus is central[3] yet presents preferential directions of motion determined by the geometry of the solid surfaces bounding the liquid meniscus. Because the die and receptor site have in the present case matching square shapes, these directions correspond to the main axes of the site. The directions are equivalent, and the associated normal shift modes are degenerate. Figure 4 shows SE simulations of the orientation of the capillary force acting on the die with no twist offset and for angular displacements ϕ of its center along arcs of constant radial offsets r_0 relative the center of the site. The orientation of the force thereby appears rather constant across almost the entire range of angular die displacement (Figure 4a). Moreover, the range of reasonably constant force orientation widens for larger offsets (Figure 4b). Across such a range of displacements, the direction of the force does not deviate significantly from that assumed along the main diagonal (i.e., for $\phi = 45°$). Hence, it is only when the center of the die lies along the main diagonal direction that the capillary force points to the center of the site. For all other positions of the die, the capillary force points instead toward the main axis closest to the center of the die. Accordingly, the preferential directions of motion represent local attractors for the self-aligning motion, whereas the center of the receptor site represents the global attractor of the trajectories and the target position of the die.[1] The geometry of the die imposes the symmetry of the capillary force field. For all biaxial shift offsets with $x_0 \neq y_0$, the trajectories of the self-aligning die describe inward spirals toward the absorbing state of the motion; i.e., they tend to cross the center of the site only toward the end of the process, as compared to every half oscillation cycle in the case of a central force field with circular symmetry. Such behavior was experimentally confirmed, as shown in section 3.5.

3.3. Twist Dynamics. Figure 5 shows the recorded modal dynamics of the individual twist mode (sketched in Figure 5a). The trajectories (Figure 5c) follow a sequence of dynamic regimes qualitatively analogous to that of the shift mode[42]

dx.doi.org/10.1021/la502831r | Langmuir 2014, 30, 13092−13102

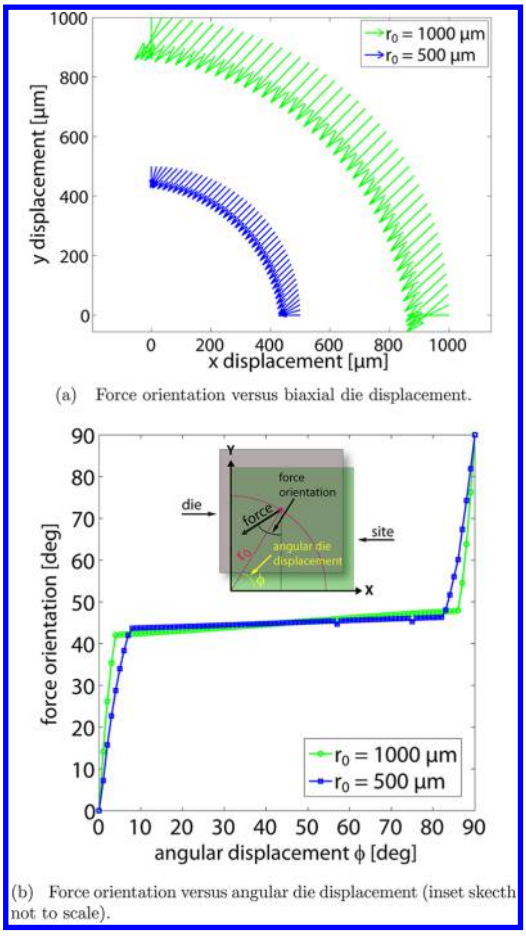

(a) Force orientation versus biaxial die displacement.

(b) Force orientation versus angular die displacement (inset sketch not to scale).

Figure 4. Orientation of the capillary force (see inset in panel b for definition) acting on a die with no twist offset and quasi-statically displaced along arcs of constant radii r_0 (500 and 1000 μm) around the center of the site, according to SE simulations.

(compare to Figure 2c). Namely, after the transient wetting regime, the angular velocity of the die increases in time and reaches a maximum in correspondence of the first zero crossing (Figure 5d) before decaying, reversing, and dissipating during the final regime of underdamped harmonic oscillations. Nonetheless, the angular velocity profile of the twist mode shows distinctive differences with the velocity profile of the shift mode. The angular acceleration of the die is found experimentally to decrease for increasing values of angular offset (cases of $\theta_0 = 15°$, 30°, and 40° are shown in panels c and d of Figure 5). Such a difference is consistent with the energetic description of the twist mode obtained by SE simulations (Figure 5b). It can be qualitatively understood by observing that, by starting the self-alignment from increasing values of angular offsets, the die is subjected to capillary torques of increasingly smaller magnitudes (Figure 5c). Moreover, the magnitude of the capillary torque is not constant, as compared to the almost constant homologous capillary force acting for relatively large shifts (Figure 2b). Rather, the restoring torque monotonously increases as the offset decreases, until reaching a maximum value in proximity of the rest position (e.g., around θ = 5° in Figure 5b). We also note that the maximum values of angular velocities ω attained for differing initial angular offsets tend to be similar (see Figure 5d and Figure S6 of the Supporting Information). Minor unintended oscillations are simultaneously observed along the shift DOFs.

For the maximum value of angular offset $\theta_0 = 45°$, the initial value of capillary torque (as well as restoring forces) is expected to be null by the competition of symmetrically opposite components and confirmed by SE (Figure 5c). Hence, a foil die landing on the liquid film with maximal misorientation with respect to the receptor site and with null biaxial offset from its center is expected to feel no torque. The die should then remain in this unstable state until some perturbation intervenes to break the rotational symmetry. Such event would prompt the rotational self-alignment of the die with the site along one direction randomly selected out of the two equivalent alternatives. Realizations of this predicted behavior were observed in dedicated experiments (see Figure S7 of the Supporting Information).

3.4. Uniaxial Shift and Twist Dynamics. The simultaneous excitation of uniaxial shift and twist modes induces sensible modifications in the trajectories described along the DOFs in comparison to the individual excitation of the same modes. Experimental evidence of mode coupling is illustrated in Figure 6, where trajectories of individually and simultaneously excited modes for treated and non-treated PEN foil dies are arranged similarly to Figure 3 described in section 3.2.

As shown by Figure 6b, the coexistence of a twist offset affects the uniaxial shift dynamics. Specifically, the time of first zero crossing along the shift DOF is retarded, and the amplitude of the overshoots in the final dynamic regime is reduced to be barely detectable. Notably, in these conditions, the time of first zero crossing along the shift tends to coincide with that along the twist mode. Such alignment of the times of first zero crossing (also seen in Figure 6e) has been repeatedly observed in all experiments of this type (see also section 3.5 and Figure S8 of the Supporting Information) and provides a hint at the mechanism of dynamical coupling between the modes.

We argue that the dynamical coupling between uniaxial shift and twist modes is rooted in a wetting issue. It is caused by the way the liquid meniscus spreads over the bottom surface of the foil die to entirely wet its farthest corner from the center of the receptor site, equivalently by the way the foil die needs to roto-translate to achieve its equilibrium pose with the least action. With reference to the significant excerpts from high-speed recordings for native PEN die shown in Figure 7, we first note that, in the presence of both uniaxial shift and twist offsets, the single corner of the foil die farthest from the center of the site can be uniquely identified (Figure 7a). Wetting by the meniscus of this corner signals the end of the self-alignment dynamics (Figure 7d), except for the decaying oscillations around the equilibrium position. The corner, along with the others, is in fact not wet by the meniscus during the transient wetting regime. To wet the farthest corner, the unpinned triple contact line on the bottom surface of the foil die should advance while assuming an increasing curvature to span the area of the corner.[16] This path is energetically more expensive than pulling the floating foil die into alignment with the edges of the receptor site. Given the initial offsets, the ensuing motion of the die turns out to be a roto-translation, whereby translation and rotation need to take place at the same time, hence, their dynamical coupling. The above arguments hold irrespective of the surface energy of the foil die, as demonstrated by the full video recordings of self-alignment experiments for native and plasma-treated PEN dies (provided in the Supporting Information). Notably, the synchronization of simultaneously excited uniaxial shift and twist modes contrasts earlier

dx.doi.org/10.1021/la502831r | Langmuir 2014, 30, 13092−13102

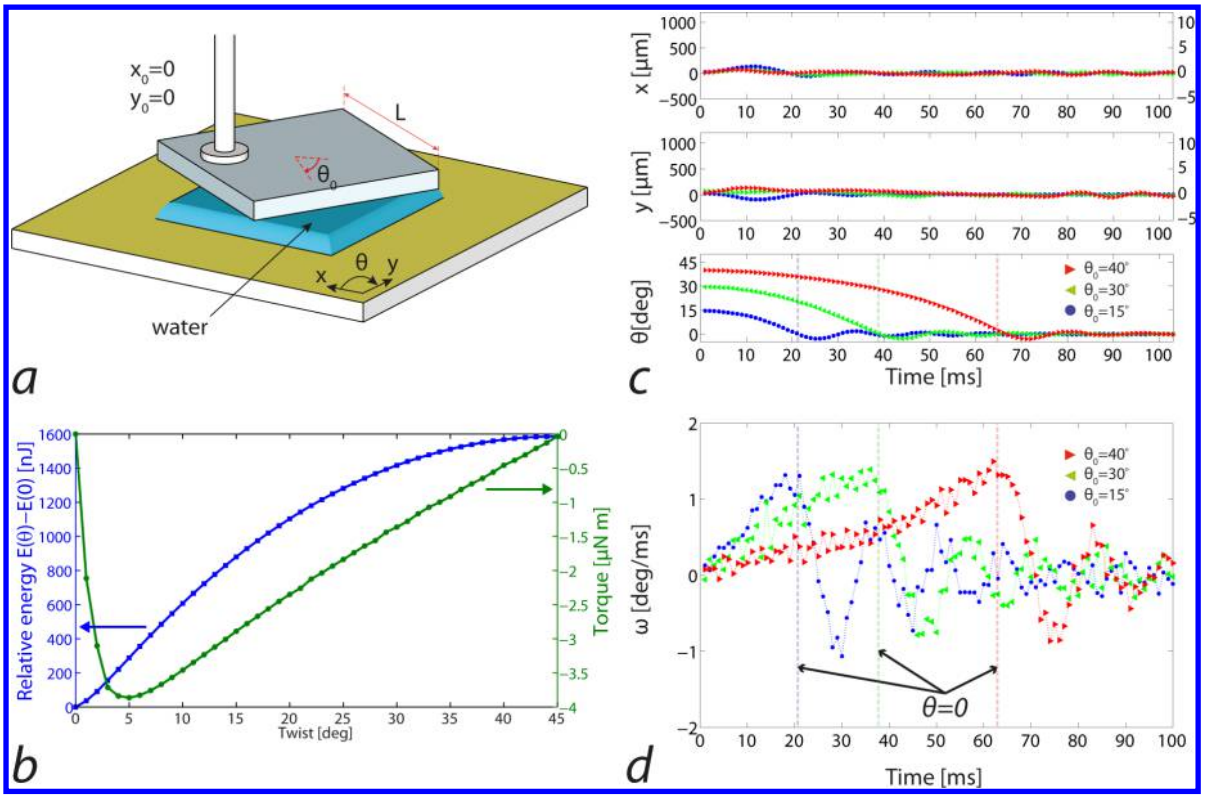

Figure 5. Twist. (a) Sketch of the experimental procedure (not to scale). (b) Relative energy landscape and capillary restoring torque predicted by quasi-static SE simulation of the twist mode. (c) Modal trajectories under twist dynamics ($x_0 = y_0 = 0$, and $\theta_0 > 0$). (d) Corresponding angular velocity ω of the die along the individually excited twist mode (see Figure S6 of the Supporting Information for additional experimental trajectories and corresponding estimates of angular acceleration $\dot{\omega}$).

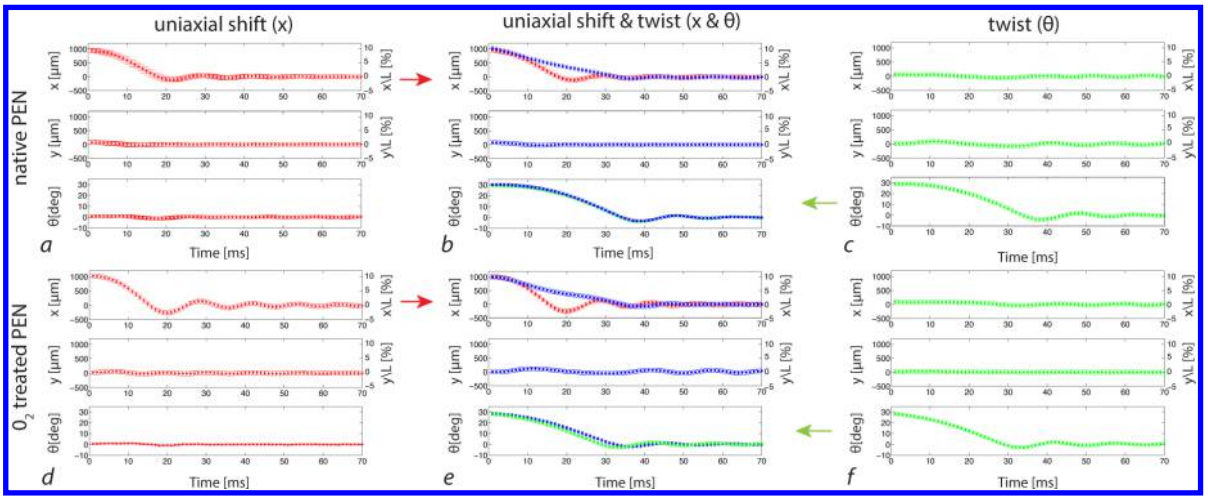

Figure 6. Coupling of uniaxial shift and twist modes. Uniaxial shift ($x_0 = 1000$ μm, $y_0 = 0$ μm, and $\theta_0 = 0°$) and twist ($x_0 = y_0 = 0$ μm, and $\theta_0 = 30°$) trajectories are shown in the first and third columns, respectively. Trajectories for the simultaneous dynamics with the same offsets ($x_0 = 1000$ μm, $y_0 = 0$ μm, and $\theta_0 = 30°$) are shown in the central column. The signature of the coupling between the modes can be observed comparing individually and simultaneously excited modes, whose trajectories are superposed in the central column (as highlighted by the horizontal arrows). Dependence of mode coupling on the surface energy of the foil die is evidenced by the difference between the case of native PEN (top row) and oxidized PEN foil die (bottom row).

reports,[1,23] where the sequentiality of shift and twist motion was instead claimed.

It should also be noted that the energetics of the uniaxial shift mode is itself affected by a twist offset and vice versa (Figure 8a). Simultaneous excitation of the modes results in increased compliance of the meniscus along the shift DOF, as evidenced in Figure 8b by a progressive decrease of the magnitude of the restoring capillary force predicted by SE simulations. Such a softening effect may play a partial role in the coupling of the modes, yet it cannot by itself explain their synchronization. SE simulations additionally predict a reciprocal softening of the twist mode caused by a shift offset (Figure 8c). Whereas the trajectories of Figure 6b do not support any noticeable effect of shift offset on twist dynamics, Figure 6e shows evidence of

dx.doi.org/10.1021/la502831r | Langmuir 2014, 30, 13092−13102

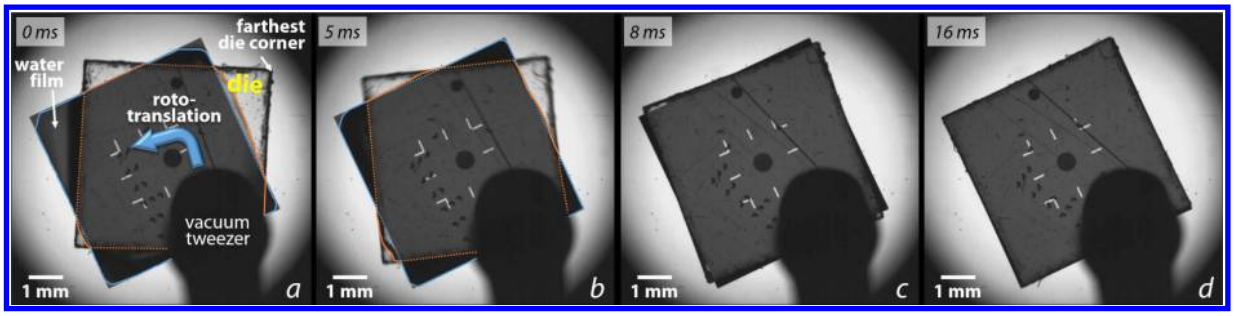

Figure 7. Sequential frames from a capillary self-alignment experiment (5×5 mm^2 native PEN foil die used in this case for full die imaging). Roto-translational motion of the transparent die toward registration with the receptor site evidenced during transient wetting in panel a. Positions of the triple contact lines of the meniscus on die and receptor site are highlighted in panels a and b. Final die pose after underdamped oscillations is shown in panel d. The full video is available in the Supporting Information.

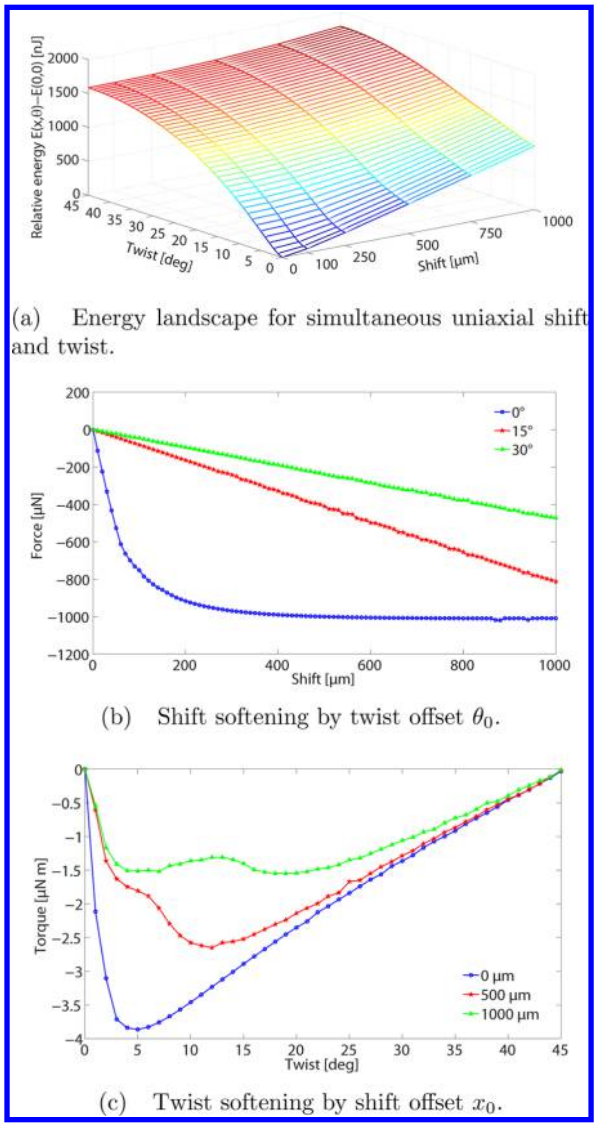

Figure 8. Energetics and reciprocal softening of uniaxial shift and twist modes from SE simulations of the experiment of Figure 6 with native PEN dies.

reciprocal mode softnening for the oxidized PEN foil. Dynamical mode coupling is therefore also affected by the surface energy of the die.

3.5. Biaxial Shift and Twist Dynamics. The experimental dynamics of capillary self-alignment under the simultaneous excitation of all three in-plane modes is depicted in Figure 9. It is observed that the presence of an offset along the twist DOF does affect the dynamics of both shift modes in a similar way. The evidence is consistent with and further supports the coupling mechanism discussed in section 3.4. The impact of the surface energy of the foil die is also confirmed, along the same lines, by the comparison of the three-dimensional trajectories shown in panels b and e of Figure 9.

The significant effect of the addition of a twist offset on the biaxial shift dynamics is further illustrated by the difference between the corresponding in-plane two-dimensional trajectories, represented in Figure 10. The simultaneous excitation of the twist mode dampens the harmonic oscillations along the shift modes. The trajectories consequently explore a smaller volume of the state space.

4. DISCUSSION

Earlier attempts at tracking the experimental dynamics of capillary self-alignment made use of components with sub-millimetric sizes.[14,48] Such studies aimed at demonstrating the repeatability of the process under differing boundary conditions by comparing initial offsets and final poses of the components. Using components of larger sizes, we were able to track the entire dynamics of self-alignment with higher spatial and temporal accuracy. The chosen transparent vehicles afford the magnified visualization of details of dewetting by contact line motion[45] and the harmonic oscillations of the components[42] hardly noticeable otherwise. Thin flat components of sizes similar to the sizes used hereby find as well applications in advanced system integration[10] and packaging.[15] Insights gained from this study can be extrapolated also to smaller geometries characterized by similar Bond numbers ($Bo = \rho g h^2/\gamma = 0.02$ hereby). Conversely, larger Bo values correspond to increasing heights of the liquid bridge, with $h \to L_c$ for $Bo \to 1$. In such conditions, the correlation between the final pose of the die and the receptor site becomes looser; besides, irreversible liquid overflow beyond the margins of the receptor site and top die tilting become increasingly likely.[32,33] These eveniences lead to failure of capillary self-alignment and make the process utterly unreliable.

The unintended and persistent oscillations detected during the experiments along nominally unexcited modes are analogous to background noise for their negligible magnitude and apparent lack of cross-correlation. We attribute the presence of such oscillations to several factors. Incidental imprecisions during system calibration and foil die release may not be excluded as well as minor defects in the shapes of dies

dx.doi.org/10.1021/la502831r | Langmuir 2014, 30, 13092−13102

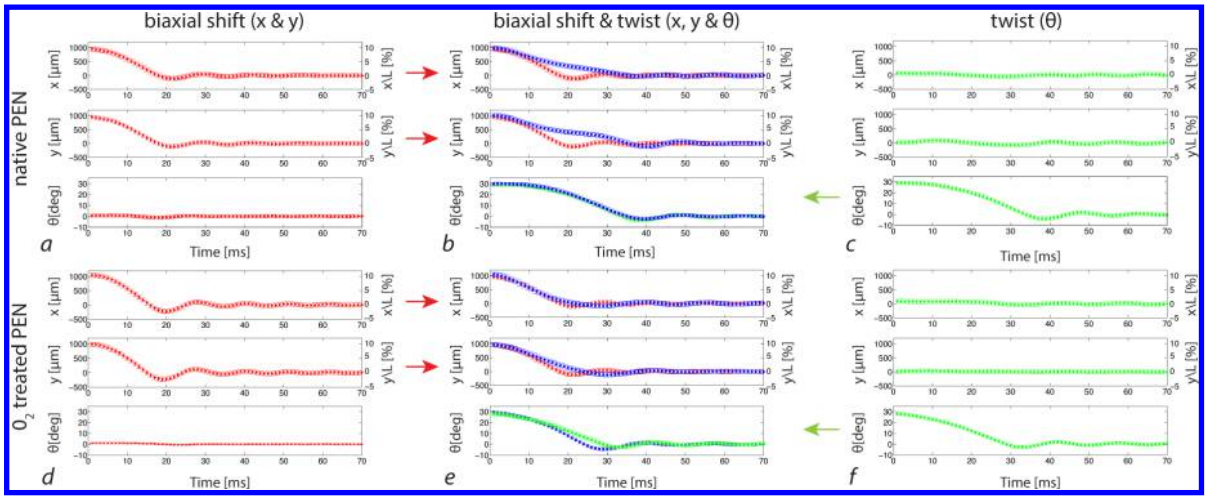

Figure 9. Coupling of biaxial shift and twist modes. Biaxial shift (x_0 = y_0 = 1000 μm, and θ_0 = 0°) and twist (x_0 = y_0 = 0 μm, and θ_0 = 30°) trajectories are shown in the first and third columns, respectively. Trajectories for the simultaneous dynamics with the same offsets (x_0 = y_0 = 1000 μm, and θ_0 = 30°) are shown in the central column. The signature of the coupling between the modes can be observed comparing individually and simultaneously excited modes, whose trajectories are superposed in the central column (as highlighted by the horizontal arrows). Dependence of mode coupling upon the surface energy of the foil die is evidenced by the difference between the case of native PEN (top row) and oxidized PEN foil die (bottom row).

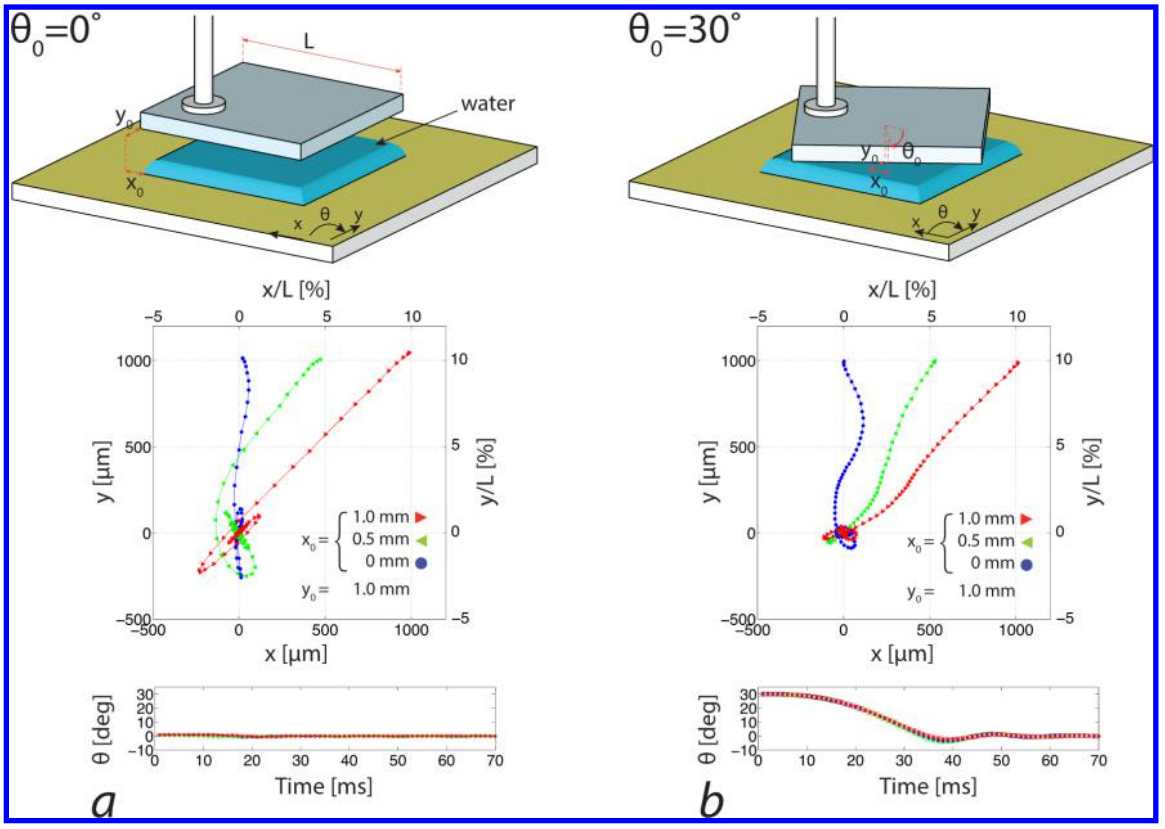

Figure 10. Complete in-plane dynamics of capillary self-alignment shown through the two-dimensional projection of the in-plane motion. (a) Biaxial shift dynamics with no twist offset. (b) Biaxial shift dynamics with twist offset.

and receptor sites. Moreover, the spatial resolution of the marker structures and the micropositioning stage are limited (see section 2.2). Despite their high relative accuracy compared to the dimensions of the dies, the markers conceded a margin of error of about 20 μm around nominal shift offsets and about 0.5° for twist offsets. Such values are rather consistent with the amplitude of the background oscillations. They, in turn, provided an additional motivation for the choice of relatively large offsets to signal the selective excitation of intended modes against the noise background. A further source of unselective mode excitation is the pinning of the meniscus on the edges of the die after spreading across its bottom surface (i.e., the transient wetting regime[42]). Although we could not entirely exclude such parasitic motions along the unexcited modes, their magnitude was negligible and bore no measurable effect on the results of the study. Incidentally, the energy transfer between

dx.doi.org/10.1021/la502831r | Langmuir 2014, 30, 13092−13102

shift modes evidenced from the envelope of the amplitude of such secondary oscillations in a previous study[42] is not confirmed here. That tentative evidence can in hindsight be attributed to a marginal simultaneous excitation of the twist mode, which remained unaccounted because of the lack of reproducible control on the rotational DOF.

As described in section 2.2, in the experiments, the top dies landed on the precoated water films of the receptor sites upon release from the vacuum tweezer. The initial offsets, including the vertical distance of the die from the film, were controlled within the afforded limits of experimental accuracy. A die-to-film gap smaller than 1.5 mm could be imposed but was ultimately avoided, because it deteriorated the precision of in-plane die prealignment. The release procedure by die free fall was hereby adopted for consistency with our previous study on uniaxial shift dynamics.[42] While we cannot in principle exclude transient tilting during the landing of the die onto the water film, especially for the largest offsets, we can exclude *a posteriori* the persistence of macroscopic tilt (i.e., discernible through the optical apparatus; see for instance the videos in the Supporting Information) of the die during its self-aligning motion, because this would have determined a rate of self-alignment failure[18,48] significantly higher than the negligible that we observed. A dedicated study of tilt dynamics may be conceivable by means of, e.g., laser range sensors and lateral mirrors, to track in real-time vertical position and tilting, respectively, of the top die during its self-alignment. Alternatively, in a collateral work,[15] we developed a die release mechanism that sidesteps the vertical free fall of the top die. Such a procedure exploits the confinement of the liquid drop within a predefined subset of the area of the receptor site. The droplet of the preset volume thereby assumes a predetermined profile, and the die is put in contact with the drop by the gripper at a controlled height before being released. This way, meniscus spreading across the bottom surface of the die mostly happens while the die is still attached to the gripper.

While outside the scope of our study, we have explicitly considered the expected dynamics of the lift DOF in the SE model. Among all modes, the lift is the first to reach equilibrium. This is expected to happen because the vertical capillary forces exerted by the confined liquid bridge are significantly larger than the lateral forces.[1,3,23] Such separation in force magnitude induces a corresponding time scale separation, whereupon the vertical relaxation of the meniscus takes place earlier than along all of the other DOFs. This is included in our numerical model (see section 2.4). By the same token, an experimental study of the lift mode would require time sampling capabilities superior to those needed to track the in-plane dynamics of the top die.

Theoretical descriptions of the dynamics of uniaxial shift described in section 3.1 have been proposed for instance by Lu and Bailey[44] and Lambert et al.[36] to estimate the characteristic damping time of the component oscillations in the final harmonic regime. In both models, the dynamics of the component is driven by the coupled physics of component motion and fluid dynamics of the liquid bridge. Newton's law describes the motion of the floating component as an oscillator, submitted to the lateral restoring capillary force and the viscous drag exerted by the liquid meniscus. The viscous drag can be derived from the Navier−Stokes equations. According to the boundary conditions, the system can be over- or underdamped. Interestingly, following the closed-form solution developed by Lambert et al.,[36] the problem was shown to depend upon only two non-dimensional numbers. The first number $\tilde{m}$ is a reduced mass, i.e., the mass of the component m normalized by half of the liquid mass. The second number α is a reduced viscosity given by $4\nu\tau/h^2$, where ν is the kinematic viscosity, h is the gap, and τ is the characteristic time. τ is determined by $(k/m)^{1/2}$, where k is the gradient of the capillary force along the shift DOF (i.e., the lateral stiffness of the meniscus in the full elastic regime[45]). For the case illustrated in Figure 2, $\tilde{m} = 2.88$ and $\alpha = 0.32$. The non-dimensional map shown in Figure S9 of the Supporting Information provides a rough estimate of the non-dimensional characteristic time τ_d between 10 and 20. This analysis correctly posits the system in the underdamped oscillatory domain in agreement with experimental observations, although outside the domain of strict analytical validity of the model.[36] The solution of the equations of the model[36] leads to $\tau_d = 16.8$, which corresponds to a dimensional characteristic time $\tau_c = 21.8$ ms, about 30% larger than the experimental value of 17 ms obtained by fitting the underdamped oscillation waveform with the function $x(t) = Ae^{-t/\tau_c}\cos(\omega t + \phi)$. The underlying reason for the quantitative discrepancy should be further investigated. The divergence between model prediction and experimental data may be attributed to the lateral capillary force, which does not follow a simple Hookean relation with uniaxial shift, in contrast to what is assumed in elastic dynamic models.[36,44] In fact, the full range of capillary restoring force was shown[45] to deviate from a fully elastic response for shift offsets relatively large compared to the sidelength, such as those adopted hereby (see section 3.1). To account for such initial displacements, the so-called mixed and full sliding regimes[45] need to be integrated in the dynamic model.

Finally, we argue that, for relatively large displacements causing unpinning of the triple contact lines,[45] contact angle hysteresis can be responsible for an actual asymmetry of the capillary forces exerted by the liquid bridge on the moving top die during its motion toward and away from the global equilibrium position. In the former case (approach to alignment), the angle formed by the moving contact lines with the adjacent substrates is likely the advancing contact angle, while in the latter case (motion away from alignment), the angle formed by the moving contact lines with the adjacent substrates is likely the receding contact angle. Because upon contact line unpinning from the edges of the bounding surfaces (i.e., in the sliding regime[45]) the capillary force is proportional to the cosine of the contact angle, the forces are expected to differ in the two cases. Additionally, dynamic contact angles are known to depend upon contact line velocity,[49] which, in turn, depends upon the initial conditions of the top die.[42] A fuller understanding of the underlying physics may be achieved upon development of a complete dynamic model of capillary self-alignment.

5. CONCLUSION

This paper presented an experimental study of the complete dynamics of capillary self-alignment along the in-plane modes of deformation of a confined liquid bridge. The modes could be synchronously and systematically analyzed with high resolution in their individual and simultaneous dynamics through selective excitation by preset initial offsets. The study confirmed earlier findings concerning the sequential dynamic regimes encountered along uniaxial self-alignment trajectories and their sensitivity to the surface energy of the floating component. The same observations could be extended to the biaxial shift dynamics in the absence of twist offset. In this case, the two-

dimensional trajectory was shown to correspond to the pointwise combination of the trajectories described along the individual orthogonal shift modes, proving that, with no twist offset, they are normal in-plane modes. The dynamics of the twist mode was shown to follow a sequence of regimes analogous to the shift modes. Coupling between the dynamics of the in-plane modes was reported in the presence of twist offset. Such dynamical coupling was attributed to a synchronization between the modes and justified by wetting and energetic arguments. The coupling was observed to reflect mutual softening of the simultaneously excited modes and to be affected by changes in surface energies.

Through the evidence reported, the study provides experimental benchmarks toward the development of a comprehensive description of fluid joints and capillary self-alignment, one that could encompass and account for both its quasi-static and dynamic properties.

■ ASSOCIATED CONTENT

Supporting Information

High-speed real-time recordings of the full self-alignment dynamics of 5 × 5 mm^2 native PEN and oxygen-plasma-treated foil dies under biaxial shift and twist offsets, together with the supplementary figures referred to in the main text. This material is available free of charge via the Internet at http://pubs.acs.org.

■ AUTHOR INFORMATION

Corresponding Author

*E-mail: massimo.mastrangeli@ulb.ac.be.

Author Contributions

†Gari Arutinov and Massimo Mastrangeli contributed equally and complementarily to this work.

Notes

The authors declare no competing financial interest.

■ ACKNOWLEDGMENTS

The work was funded through the Marie Curie ITN FlexSmell Project 238454 and the Interuniversity Attraction Poles Programme (IAP 7/38 MicroMAST) initiated by the Belgian Science Policy Office. The authors thank Jaap den Toonder, Andreas Dietzel, and Bernardo Innocenti for insightful discussions.

■ REFERENCES

(1) Berthier, J.; Brakke, K.; Grossi, F.; Sanchez, L.; Di Cioccio, L. Self-alignment of silicon chips on wafers: A capillary approach. *J. Appl. Phys.* **2010**, *108*, 054905.

(2) Broesch, D. J.; Dutka, F.; Frechette, J. Curvature of capillary bridges as a competition between wetting and confinement. *Langmuir* **2013**, *29*, 15558−15564.

(3) Lienemann, J.; Greiner, A.; Korvink, J. G.; Xiong, X.; Hanein, Y.; Böhringer, K. F. In *Sensor Update 13*; Baltes, H., Fedder, G. K., Korvink, J., Eds.; Wiley-VCH: Weinheim, Germany, 2004; Chapter Modeling, Simulation, and Experimentation of a Promising New Packaging Technology: Parallel Fluidic Self-Assembly of Microdevices, pp 3−43.

(4) Adamson, A. W.; Gast, A. P. *Physical Chemistry of Surfaces*; Wiley-Interscience: Hoboken, NJ, 1997.

(5) Israelachvili, J. N. *Intermolecular and Surface Forces*; Academic Press: Waltham, MA, 2011.

(6) Crane, N. B.; Onen, O.; Carballo, J.; Ni, Q.; Guldiken, R. Fluidic assembly at the microscale: Progress and prospects. *Microfluid. Nanofluid.* **2013**, *14*, 383−419.

(7) *Surface Tension in Microsystems*; Lambert, P., Ed.; Springer: New York, 2013.

(8) Jacobs, H. O.; Tao, A. R.; Schwartz, A.; Gracias, D. H.; Whitesides, G. M. Fabrication of a cylindrical display by patterned assembly. *Science* **2002**, *296*, 323−325.

(9) Knuesel, R. J.; Jacobs, H. O. Self-assembly of microscopic chiplets at a liquid−liquid−solid interface forming a flexible segmented monocrystalline solar cell. *Proc. Natl. Acad. Sci. U. S. A.* **2010**, *107*, 993−998.

(10) Fukushima, T.; Iwata, E.; Ohara, Y.; Murugesan, M.; Bea, J.; Lee, K.; Tanaka, T.; Koyanagi, M. Multichip-to-wafer three-dimensional integration technology using chip self-assembly with excimer lamp irradiation. *IEEE Trans. Electron Devices* **2012**, *59*, 2956−2963.

(11) Leong, T. G.; Zarafshar, A. M.; Gracias, D. H. Three-dimensional fabrication at small size scales. *Small* **2010**, *6*, 792−806.

(12) Mastrangeli, M. In *Surface Tension in Microsystems*; Lambert, P., Ed.; Springer: New York, 2013; Chapter Surface Tension-Driven Self-Assembly, pp 227−253.

(13) Gauthier, M.; Régnier, S. *Robotic Micro-assembly*; John Wiley and Sons: Hoboken, NJ, 2011.

(14) Sariola, V.; Jääskeläinen, M.; Zhou, Q. Hybrid microassembly combining robotics and water droplet self-alignment. *IEEE Trans. Rob.* **2010**, *26*, 965−977.

(15) Arutinov, G.; Mastrangeli, M.; Smits, E. C. P.; Van Heck, G.; den Toonder, J. M. J.; Dietzel, A. Foil-to-foil system integration through capillary self-alignment directed by laser patterning. *J. Microelectromech. Syst.* **2014**, DOI: 10.1109/JMEMS.2014.2321013.

(16) Mastrangeli, M.; Ruythooren, W.; Celis, J.-P.; van Hoof, C. Challenges for capillary self-assembly of microsystems. *IEEE Trans. Compon., Packag., Manuf. Technol.* **2011**, *1*, 133−149.

(17) Broesch, D. J.; Frechette, J. From concave to convex: Capillary bridges in slit pore geometry. *Langmuir* **2012**, *28*, 15548−15554.

(18) Sato, K.; Itoa, K.; Hata, S.; Shimokohbe, A. Self-alignment of microparts using liquid surface tension—Behavior of micropart and alignment characteristics. *Precis. Eng.* **2003**, *27*, 42−50.

(19) Gracias, D. H.; Tien, J.; Breen, T. L.; Hsu, C.; Whitesides, G. M. Forming electrical networks in three dimensions by self-assembly. *Science* **2000**, *289*, 1170−1172.

(20) Mastrangeli, M.; Jacot-Descombes, L.; Gullo, M. R.; Brugger, J. Liquid-filled sealed MEMS capsules fabricated by fluidic self-assembly. *IEEE Int. Conf. Micro Electro Mech. Syst., 27th* **2014**, 56−59.

(21) Patra, S. K.; Lee, Y. C. Quasi-static modeling of the self-alignment mechanism in flip-chip soldering. Part I: Single solder joint. *J. Electron. Packag.* **1991**, *113*, 337−342.

(22) van Veen, N. Analytical derivation of the self-alignment motion of flip chip soldered components. *J. Electron. Packag.* **1999**, *121*, 116−121.

(23) Berthier, J.; Brakke, K. *The Physics of Microdroplets*; John Wiley and Sons and Scrivener Publishing: Hoboken, NJ, 2012.

(24) Gao, S.; Zhou, Y. Self-alignment of micro-parts using capillary interaction: Unified modeling and misalignment analysis. *Microelectron. Reliab.* **2013**, *53*, 1137−1148.

(25) Mastrangeli, M.; Valsamis, J.-B.; van Hoof, C.; Celis, J.-P.; Lambert, P. Lateral capillary forces of cylindrical fluid menisci: A comprehensive quasi-static study. *J. Micromech. Microeng.* **2010**, *20*, 075041.

(26) Berthier, J.; Mermoz, S.; Brakke, K.; Sanchez, L.; Frétigny, C.; Di Cioccio, L. Capillary self-alignment of polygonal chips: a generalization for the shift-restoring force. *Microfluid. Nanofluid.* **2013**, *14*, 845−858.

(27) Takei, A.; Matsumoto, K.; Shimoyama, I. Capillary torque caused by a liquid droplet sandwiched between two plates. *Langmuir* **2010**, *26*, 2497−2504.

(28) Broesch, D. J.; Shiang, E.; Frechette, J. Role of substrate aspect ratio on the robustness of capillary alignment. *Appl. Phys. Lett.* **2014**, *104*, 081605.

(29) Mastrangeli, M.; Abbasi, S.; Varel, C.; van Hoof, C.; Celis, J.-P.; Böhringer, K. F. Self-assembly from milli- to nanoscales: Methods and applications. *J. Micromech. Microeng.* **2009**, *19*, 083001.

(30) Ahn, D. H.; Lee, J.; Yoo, C. D.; Kim, J.-S. Influence of pad shape on self-alignment in electronic packaging. *J. Electron. Mater.* **2006**, *35*, 411−415.
(31) Routa, I.; Chang, B.; Shah, A.; Zhou, Q. Surface tension-driven self-alignment of microchips on low-precision receptors. *J. Microelectromech. Syst.* **2013**, *23*, 819−828.
(32) Scott, K. L.; Howe, R. T.; Radke, C. J. Model for micropart planarization in capillary-based microassembly. *Transducers '03, Int. Conf. Solid-State Sens., Actuators Microsyst., Dig. Tech. Pap., 12th* **2003**, 1319−1322.
(33) Abbasi, S.; Zhou, A.; Baskaran, R.; Böhringer, K. F. Part tilting in capillary-based self-assembly: Modeling and correction methods. *IEEE Int. Conf. Micro Electro Mech. Syst., 21st* **2008**, 1060−1063.
(34) Kim, J.-M.; Yasuda, K.; Fujimoto, K. Resin self-alignment processes for self-assembly systems. *J. Electron. Packag.* **2005**, *127*, 18−24.
(35) Fennell, B.; Lee, S.; Baldwin, D. F. Translation solder self-alignment mechanics modeling for a flip chip in the presence of a viscous fluid. *J. Electron. Packag.* **2010**, *132*, 041013.
(36) Lambert, P.; Mastrangeli, M.; Valsamis, J.-B.; Degrez, G. Spectral analysis and experimental study of lateral capillary dynamics for flip-chip applications. *Microfluid. Nanofluid.* **2010**, *9*, 797−807.
(37) Arutinov, G.; Smits, E. C. P.; Mastrangeli, M.; Van Heck, G.; van den Brand, J.; Schoo, H. F. M.; Dietzel, A. Capillary self-alignment of mesoscopic foil components for sensor-systems-in-foil. *J. Micromech. Microeng.* **2012**, *22*, 115022.
(38) Tsai, C. G.; Hsieh, C. M.; Yeh, J. A. Senf-alignment of microchips using surface tension and solid edge. *Sens. Actuators, A* **2007**, *139*, 343−349.
(39) Chang, B.; Shah, A.; Routa, I.; Lipsanen, H.; Zhou, Q. Low-height sharp edged patterns for capillary self-alignment assisted hybrid microassembly. *J. Micro-Bio Rob.* **2014**, *9*, 1−10.
(40) Chang, B.; Routa, I.; Sariola, V.; Zhou, Q. Self-alignment of RFID dies on four-pad patterns with water droplet for sparse self-assembly. *J. Micromech. Microeng.* **2011**, *21*, 095024.
(41) Chang, B.; Shah, A.; Routa, I.; Lipsanen, H.; Zhou, Q. Surface-tension driven self-assembly of microchips on hydrophobic receptor sites with water using forced wetting. *Appl. Phys. Lett.* **2012**, *101*, 114105.
(42) Arutinov, G.; Mastrangeli, M.; Smits, E. C. P.; Schoo, H. F. M.; Brugger, J.; Dietzel, A. Dynamics of capillary self-alignment for mesoscopic foil devices. *Appl. Phys. Lett.* **2013**, *102*, 144101.
(43) Kim, J.-M.; Shin, Y. E.; Fujimoto, K. Dynamic modeling for resin self-alignment mechanism. *Microelectron. Reliab.* **2004**, *44*, 983−992.
(44) Lu, H.; Bailey, C. Dynamic analysis of flip-chip self-alignment. *IEEE Trans. Adv. Packag.* **2005**, *28*, 475−480.
(45) Mastrangeli, M.; Arutinov, G.; Smits, E. C. P.; Lambert, P. Modeling capillary forces for large displacements. *Microfluid. Nanofluid.* **2014**, DOI: 10.1007/s10404-014-1469-9.
(46) Brakke, K. The surface evolver. *Exp. Math.* **1992**, *1*, 141−165.
(47) Lanczos, C. *The Variational Principles of Mechanics*; Dover: Mineola, NY, 1970.
(48) Sato, K.; Lee, K.; Nishimura, M.; Okutsu, K. Self-alignment and bonding of microparts using adhesive droplets. *IEEE Trans. Electron. Packag. Manuf.* **2007**, *8*, 75−79.
(49) Snoeijer, J. H.; Andreotti, B. Moving contact lines: Scales, regimes and dynamical transitions. *Annu. Rev. Fluid Mech.* **2013**, *45*, 269−292.